



**HAL**  
open science

# Non-linear composite voxels for FFT-based explicit modeling of slip bands: application to basal channeling in irradiated Zr alloys

Aldo Marano, Lionel Gélébart

## ► To cite this version:

Aldo Marano, Lionel Gélébart. Non-linear composite voxels for FFT-based explicit modeling of slip bands: application to basal channeling in irradiated Zr alloys. 2020. hal-02484451

**HAL Id: hal-02484451**

**<https://hal.science/hal-02484451>**

Preprint submitted on 19 Feb 2020

**HAL** is a multi-disciplinary open access archive for the deposit and dissemination of scientific research documents, whether they are published or not. The documents may come from teaching and research institutions in France or abroad, or from public or private research centers.

L'archive ouverte pluridisciplinaire **HAL**, est destinée au dépôt et à la diffusion de documents scientifiques de niveau recherche, publiés ou non, émanant des établissements d'enseignement et de recherche français ou étrangers, des laboratoires publics ou privés.

# Non-linear composite voxels for FFT-based explicit modeling of slip bands: application to basal channeling in irradiated Zr alloys

Aldo Marano<sup>a,b</sup>, Lionel Gélébart<sup>a,\*</sup>

<sup>a</sup>*DEN- Service de Recherches Métallurgiques Appliquées, CEA, Université Paris-Saclay, F-91191, Gif-sur-Yvette, France*

<sup>b</sup>*MINES ParisTech, PSL Research University, MAT - Centre des matériaux, CNRS UMR 7633, BP 87 9103 Evry, France*

---

## Abstract

Explicitly modeling slip bands is a promising method to simulate the consequences of intragranular plastic slip localization on the behavior of strongly localizing crystals such as irradiated metals. In this study, we propose a very efficient framework to implement this modeling strategy based on a massively parallel FFT-based solver enhanced with composite voxels to simulate polycrystals with a regular lamellar structure alternating plastic slip bands embedded within larger elastic bands. To this end, generic composite voxel models have been formulated and implemented, allowing to extend the approach to any type of constitutive behavior in the future. In particular, we show that laminate composite voxels are particularly well suited to improve standard FFT-based solvers in this context, and enable to run polycrystalline simulations accurately accounting for slip bands whose width is two orders of magnitude below the grain size. To demonstrate the potential of this approach, we apply it to an idealized material designed to approximate basal channeling in irradiated textured Zr alloys. Varying the width and the spacing of the modeled slip bands, we show that it allows to capture the increase of grain boundary normal stress concentrations or the enhanced Bauschinger effect induced by an increased localization of plastic slip.

---

\*Corresponding author

*Email addresses:* [aldo.marano@mines-paristech.fr](mailto:aldo.marano@mines-paristech.fr) (Aldo Marano),  
[lionel.gelebart@cea.fr](mailto:lionel.gelebart@cea.fr) (Lionel Gélébart)

*Keywords:* Slip localization, Crystal plasticity, FFT methods, Composite Voxels, Irradiated metals

---

## 1. Introduction

An accurate description of the intrinsically heterogeneous nature of plastic slip is fundamental to the understanding of the mechanical behavior of crystalline materials. From gliding dislocations to millimetric slip band bundles, the wide range of deformation structures yielded by plastic slip over several length scale have been extensively described by [Neuhäuser \(1983\)](#) and [Jaoul \(1964\)](#). At the relevant scale for continuum mechanics, the elementary slip structure is the well known *slip band*, a thin layer of localized plastic slip parallel to one of the most favorable slip plane of the crystal lattice, and plays a fundamental role in the mechanical behavior of crystals. Microscopic slip bands have been shown to precede and cause macroscopic strain localization in ductile metallic crystals ([Korbel and Martin \(1986\)](#); [Korbel et al. \(1986\)](#); [Korbel and Martin \(1988\)](#)) and to play a role in the initiation of fatigue crack along slip planes ([Bridier et al. \(2008\)](#); [Ahmed et al. \(2001\)](#)). Besides, strain localization within intense slip bands has been correlated to a low or negative work-hardening in metals exhibiting local softening mechanisms such as Titanium alloys ([Neeraj et al. \(2000\)](#); [Lai et al. \(2015\)](#)), hydrogen enriched austenitic steels ([Ulmer and Altstetter \(1991\)](#)) or quench-hardened aluminum [Mori and Meshii \(1969\)](#) and gold [Bapna and Meshii \(1974\)](#), or highly irradiated metals ([Sharp \(1972\)](#); [Onimus et al. \(2004\)](#); [Byun et al. \(2006\)](#)).

In the latter, a particularly severe localization is observed: irradiation induced crystal defects can be annihilated by gliding dislocations, resulting into a strong local softening promoting further slip on already active slip planes. This dislocation channeling mechanism results in defect-free channels associated to a very intense plastic slip, called *clear channels*. Among the consequences, besides the pronounced loss of ductility observed in irradiated metals ([Pokor et al. \(2004\)](#)), this localization is thought to be one of the causes of the irradiation assisted corrosion (intergranular) cracking (IASCC) phenomenon in irradiated steels ([Jiao and Was \(2011\)](#)), and the increased Bauschinger effect observed in irradiated Zr alloys by [Wisner et al. \(1994\)](#) is attributed by [Luft \(1991\)](#) and [Onimus and Bechade \(2009\)](#) to the strain incompatibilities generated by clear channels formation.

A proper modeling of slip bands appears then as an essential requirement to address the numerical simulation of these phenomena. Extensive studies have been devoted to simulate slip localization in crystals (Dao and Asaro (1996a,b); Sluys and Estrin (2000)). In the case of irradiated metals, models based on softening classical crystal plasticity (CCP) have been developed (Patra and McDowell (2012, 2016); Barton et al. (2013); Xiao et al. (2015); Erinoshov and Dunne (2015); Hure et al. (2016)) to conduct full-field simulations of strain localization. If intense localization bands are successfully captured, these models fail to reproduce realistic slip bands networks. Indeed, Asaro and Rice (1977) showed that CCP equations coupled with a perfect plastic or softening behaviour leads to unstable plastic flow with localization bands. However, their analysis predicts two possible bifurcation modes: slip bands and kink bands. It has been recently demonstrated that they are equivalent in all CCP models and thus form in equal quantities in polycrystalline simulations assuming initially homogeneous grains leading in particular to non-physical amounts of kink bands (Marano et al. (2019)). Even though Forest (1998) has evidenced that this fundamental shortcoming can be overcome with higher order continuum based crystal plasticity, the development of an efficient framework to accurately simulate the physical characteristics (width, spacing, local strain...) of slip bands networks is still an open problem that will require long-term efforts.

On the contrary, these features can be easily accounted for when explicitly (geometrically) modeling slip bands. This represents a more pragmatic approach aimed at gaining insight into the effect of increased localization on the mechanical behavior of irradiated metals. Sauzay et al. (2010) have modeled one or two clear channels between a free surface and a grain boundary within a finite element mesh, embedded in a hard matrix, and have shown that slip band width is the most influential parameter for the stress induced on the grain boundary. Pushing the approach further, Zhang et al. (2010) have modeled slip band formation in the  $\alpha$  phase of duplex Ti-6Al-4V by prescribing a potential slip band pattern of fixed width and spacing: material softening is allowed only inside the bands, triggering slip localization in the prescribed areas. They could qualitatively reproduce the slip band behavior observed on SEM micrographs from experiments at various strain levels. However, their study is restricted to two-dimensional simulations with a small number of grains. 3D polycrystalline simulations of realistic slip band patterns are more challenging from a computational point of view. For instance, as the typical width of clear bands is one hundred times lower than

the usual grain size in nuclear industry alloys ( $\sim 40$  nm to  $80$  nm vs.  $\sim 8$   $\mu\text{m}$  to  $10$   $\mu\text{m}$  in irradiated Zr alloys [Onimus et al. \(2004\)](#)), the size of elements should be at least equal or smaller, requiring millions of elements per grain. Hence simulating a representative number of grains with explicit slip bands comes with a colossal computational cost.

To get around this issue, FFT-based solvers, that have known extensive developments since the pioneer work of [Moulinec and Suquet \(1998\)](#), have proven to be more efficient than FEM solvers [Robert and Mareau \(2015\)](#) and can be efficiently parallelized, seem an ideal candidate. However, as they operate on regular grids, standard FFT-based solvers would require high resolutions to accurately simulate slip bands. The recent development of the composite voxel technique initially introduced for linear elasticity by [Gélébart and Ouaki \(2015\)](#) and [Kabel et al. \(2015\)](#), and extended to inelastic materials by [Kabel et al. \(2017\)](#) and [Mareau and Robert \(2017\)](#) allow to circumvent this difficulty. They allow to replace the constitutive behavior of a voxel crossed by an interface with an homogenized behavior accounting for the phases within it and possibly some geometrical informations regarding their arrangement in the voxel. They strongly increase both the accuracy of the simulated effective properties and the local quality of the strain and stress fields. As a result, they allow to achieve the same degree of precision as classical FFT based methods with a reduced resolution, hence reducing computational time and memory requirements. In addition, they have been recently applied by [Charière et al. \(2020\)](#) to hollow glass microspheres/polypropylene composites, showing to be particularly well-suited for microstructures with very thin heterogeneities, compared to the unit cell size. Thus, they should be of prime interest for explicit slip band modeling, which involves a high number of generally thin bands within the unit cell.

Thus, in this paper, we propose an efficient and generic numerical framework based on a massively parallel FFT-based solver enhanced with composite voxels designed for realistic polycrystalline simulations of explicit slip band networks. We then show its ability to study the influence of dislocation channeling in irradiated alloys with a specific focus on slip localization induced kinematic hardening and grain boundary stress concentrations. This paper is organized as follow: [section 2](#) briefly presents our FFT implementation and details the non-linear generic composite voxel models that have been implemented in the context of small strains. [Section 3](#) describes the generation of polycrystalline unit cells containing explicit slip band patterns discretized with composite voxels, as well as the characteristics and material

behavior of the model material selected for our application: an approximation of irradiated textured Zr alloys used in the nuclear industry. 3D polycrystalline simulations are shown in [section 4](#) and discussed in [section 5](#) to illustrate the efficiency of our numerical framework and analyze its prediction in terms of grain boundary normal stresses and macroscopic kinematic hardening, as a function of the slip band network geometrical characteristics (width and spacing).

## 2. Methods

### 2.1. FFT-based solver

Simulations are performed using the in-house FFT solver `AMITEX_FFTP`<sup>1</sup>. It relies on the classical basic scheme of [Moulinec and Suquet \(1998\)](#), consisting in solving iteratively the following equations until mechanical equilibrium is reached:

$$\begin{aligned} \boldsymbol{\tau}(\mathbf{x}_i) &= \boldsymbol{\sigma}(\mathbf{x}_i) - \underline{\underline{\mathbf{A}}}^0 : \underline{\underline{\boldsymbol{\varepsilon}}}(\mathbf{x}_i) \quad \forall \mathbf{x}_i \in \Omega & (1) \\ \hat{\underline{\underline{\boldsymbol{\varepsilon}}}}^{k+1}(\boldsymbol{\xi}_i) &= \hat{\underline{\underline{\mathbf{T}}}}^0 : \hat{\underline{\underline{\boldsymbol{\tau}}}}^k, \quad \forall \boldsymbol{\xi}_i \neq 0 \quad \hat{\underline{\underline{\boldsymbol{\varepsilon}}}}^{k+1}(0) = E & (2) \end{aligned}$$

over a periodic unit cell  $\Omega$  discretized by a regular grid of  $N$  voxels ( $N = N_1 \times N_2 \times N_3$ ), where  $\boldsymbol{\tau}$ ,  $\boldsymbol{\sigma}$  and  $\underline{\underline{\boldsymbol{\varepsilon}}}$  are respectively the polarisation, Cauchy stress and strain tensors in real space,  $\hat{\underline{\underline{\boldsymbol{\varepsilon}}}}$  and  $\hat{\underline{\underline{\boldsymbol{\tau}}}}$  are the strain and polarisation tensor in Fourier space,  $\mathbf{x}_i$  and  $\boldsymbol{\xi}_i$  are the grid points coordinates respectively in real space and in Fourier space, and  $\underline{\underline{\mathbf{A}}}$  is the elastic stiffness tensor of a reference isotropic linear elastic material. Thanks to the local formulation of both [eqs. \(1\) and \(2\)](#) in real (resp. Fourier) space, their resolution is implemented in a massively parallel fashion in the solver `AMITEX_FFTP`.

$\hat{\underline{\underline{\mathbf{T}}}}^0$  is the modified discrete operator proposed by [Willot \(2015\)](#), and has been shown to be equivalent to a discretization of the unit cell with cubic linear finite elements with reduced integration ([Schneider et al. \(2017\)](#)).

Besides, Anderson's convergence acceleration technique is applied to this fix-point scheme: every three iterations, this technique is applied to propose an accelerated solution using four pairs of residual-solution obtained from previous iterations. Its principle is detailed in [Anderson \(1965\)](#), and its implementation in `AMITEX_FFTP` in [Chen et al. \(2019\)](#). This algorithm drastically enhance the convergence of the basic scheme. Besides, for

---

<sup>1</sup><http://www.maisondelasimulation.fr/projects/amitex/html/>

non-linear materials simulation, compared to a Newton-Raphson implementation (Gélébart and Mondon-Cancel (2013)), it does not require the tedious evaluation of the tangent behavior.

## 2.2. Non-linear composite voxel models

FFT-based solver operate on voxelwise constant fields defined on regular grids. At each iteration, the evaluation of the stress field over each voxel (eq. (1)) requires the integration of the constitutive relations of the material lying in the voxel. However, when the voxel is crossed by interfaces the choice is no longer unique. Most FFT-based codes use the constitutive relation of the phase lying at the center of the voxel, resulting in a poor description of the microstructure close to interfaces. Alternatively, a more sophisticated choice consists in using an homogenization rule for the behavior of the voxel, accounting for the different phases and their distribution in the voxel, which is called a composite voxel (CV).

The first composite voxel models have been introduced by Gélébart and Ouaki (2015) and Kabel et al. (2014) that used classical homogenization rules for two-phases elastic materials : Voigt and Reuss bounds, and an elastic laminate approximation. In those cases, the effective properties of the composite voxel can be computed directly using their analytical expression. Mareau and Robert (2017) used these linear formulations to extend this technique to inelastic materials, by considering the effective CV inelastic strain as an eigenstrain. Non-linear CV models formulated as non-linear systems solved with an iterative Newton-Raphson procedure have also been developed for two-phases hyper-elastic materials (Kabel et al. (2016)) and inelastic materials (Kabel et al. (2017)), requiring the evaluation of local tangent behaviors. In this paper, we propose a unified and generic formulation allowing to use non-linear CV with any non-linear behavior for any arbitrary number of phases ( $N_\phi$ ) and any homogenization rule, and apply it too the three classical CV models used by the mentioned authors.

CV models can be seen as a constitutive relation linking the average stress over the composite voxel (eq. (3)) to: the local stress and strain state:  $\{\underline{\sigma}_i, \underline{\epsilon}_i\}_{1 \leq i \leq N_\phi}$ , the coefficients  $\mathbf{C}_{CV}$  that are specific to the chosen homogenization rule  $\mathcal{H}$ , containing at least the phases volume fractions  $f_i$  and the average strain imposed over the CV  $\underline{\epsilon}_{CV}$  (eq. (4)). Indeed, at each iteration, the FFT-based scheme prescribes the strain over each voxel through eq. (2),

which becomes  $\underline{\boldsymbol{\epsilon}}_{CV}$  for the CV.

$$\underline{\boldsymbol{\sigma}}_{CV} = \sum_{i=1}^{N_\phi} f_i \underline{\boldsymbol{\sigma}}_i \quad (3)$$

$$\underline{\boldsymbol{\epsilon}}_{CV} = \sum_{i=1}^{N_\phi} f_i \underline{\boldsymbol{\epsilon}}_i \quad (4)$$

More precisely, for a CV with an arbitrary number of phases  $N_\phi$ , the problem has  $2 \times 6N_\phi$  unknowns  $\{\underline{\boldsymbol{\sigma}}_i, \underline{\boldsymbol{\epsilon}}_i\}_{1 \leq i \leq N_\phi}$ . The local stress and strain state of each phase must verify the local constitutive relations (eq. (5)) providing  $6N_\phi$  equations. Hence, the homogenization rule  $\mathcal{H}$  must represent a set of  $6N_\phi$  equations so that the system eqs. (5) and (6) is a non-linear system of  $2 \times 6N_\phi$  equations.

$$\underline{\boldsymbol{\sigma}}_i = \mathcal{F}_i(\underline{\boldsymbol{\epsilon}}_i, \boldsymbol{\alpha}_i, \mathbf{C}_i) \quad \forall i/1 \leq i \leq N_\phi \quad (5)$$

$$\mathcal{H}(\{\underline{\boldsymbol{\sigma}}_i, \underline{\boldsymbol{\epsilon}}_i\}_{1 \leq i \leq N_\phi}; \underline{\boldsymbol{\epsilon}}_{CV}, \mathbf{C}_{CV}) = 0 \quad (6)$$

In practice eq. (5) is used to compute the  $\{\sigma_i\}_{1 \leq i \leq N_\phi}$  from the  $\{\epsilon_i\}_{1 \leq i \leq N_\phi}$  and eq. (3) is used to compute the CV stress as a post-processing when the local stress state are known. Thus, the problem reduces to a  $6N_\phi$  unknowns problem with the  $6N_\phi$  equations represented by eq. (7).

$$\mathcal{H}^0(\{\epsilon_i\}_{1 \leq i \leq N_\phi}; \underline{\boldsymbol{\epsilon}}_{CV}, \mathbf{C}_{CV}) = 0 \quad (7)$$

Defining a composite voxel model consists then in proposing a specific homogenization rule  $\mathcal{H}^0$ , and its associated coefficients  $\mathbf{C}_{CV}$ . We have considered three different rules in our work, following Gélébart and Ouaki (2015); Kabel et al. (2015). They are described below.

**Voigt CV:**  $\mathcal{H}$  represents the Voigt approximation: the strain state is supposed to be homogeneous in the voxel. Hence, by denoting  $\mathcal{H}_i^0$  the  $i^{th}$  equation of  $\mathcal{H}^0$ , eq. (7) takes here the form:

$$\underline{\boldsymbol{\epsilon}}_i - \underline{\boldsymbol{\epsilon}}_{CV} = 0 \quad \forall i/1 \leq i \leq N_\phi \quad (8)$$

Equation (8) is solved directly by prescribing all local strain states to  $\underline{\boldsymbol{\epsilon}}_{CV}$ . The constraint defined by eq. (4) is then automatically verified. All the local strain states  $\underline{\boldsymbol{\epsilon}}_i$  are known and thus also all stress states  $\underline{\boldsymbol{\sigma}}_i$  through the constitutive relations (eq. (5)). Finally the macroscopic stress state can be evaluated using eq. (3).  $\mathbf{C}_{CV}$  reduces to the phases volume fractions  $\{f_i\}_{1 \leq i \leq N_\phi}$ .

Voigt approximation provides the stiffest bound for the composite voxel constitutive relation.

**Reuss CV:**  $\mathcal{H}$  represents the Reuss approximation: the stress state is supposed to be homogeneous in the voxel. Hence, eq. (7) takes the form:

$$\underline{\boldsymbol{\sigma}}_i - \underline{\boldsymbol{\sigma}}_{CV} = 0 \quad \forall i/1 \leq i \leq N_\phi \quad (9)$$

If eq. (9) is verified, the constraint defined by eq. (3) is then automatically verified, but the constraint on the average strain eq. (4) is not. As  $\underline{\boldsymbol{\sigma}}_{CV}$  is not prescribed by the FFT-based scheme (evaluated as a post-treatment with eq. (3)), we solve in practice the following set of  $6N_\phi$  equations for  $\mathcal{H}^0$ :

$$\underline{\boldsymbol{\sigma}}_i - \underline{\boldsymbol{\sigma}}_1 = 0 \quad \forall i/2 \leq i \leq N_\phi \quad (10)$$

$$\sum_{i=1}^{N_\phi} f_i \underline{\boldsymbol{\varepsilon}}_i - \underline{\boldsymbol{\varepsilon}}_{CV} = 0 \quad (11)$$

$\mathcal{C}_{CV}$  reduces to the phases volume fractions  $\{f_i\}_{1 \leq i \leq N_\phi}$ . Reuss approximation provides the softer bound for the composite voxel constitutive relation.

**Laminate CV:** they consist in a linear approximation of the interface between phases, which is assumed to be a plane  $P$  with normal direction  $\mathbf{N}$ . The voxel is supposed to behave as an infinite laminate material. The solution of this classical mechanical problem are phasewise constant fields, that must verify the following relation:

$$\underline{\boldsymbol{\sigma}}_{CV}^N - \underline{\boldsymbol{\sigma}}_i^N = 0 \quad \forall i/1 \leq i \leq N_\phi \quad (12)$$

$$\underline{\boldsymbol{\varepsilon}}_{CV}^P - \underline{\boldsymbol{\varepsilon}}_i^P = 0 \quad \forall i/1 \leq i \leq N_\phi \quad (13)$$

Superscripts  $N$  and  $P$  denote respectively the normal and in-plane part (3 components each) of a tensor with respect to the plane  $P$ . Equation (12) states that the local stress fields must verify the continuity of the traction vector at the interface between the phases, and eq. (13) states that local strain fields must be compatible.

Equation (13) is solved directly by prescribing all in-plane components of the local strain states to  $\underline{\boldsymbol{\varepsilon}}_{CV}^P$ . The in-plane components of the local stress tensors are computed from eq. (5). Similarly to the derivation of the equation system for Reuss CV, as  $\underline{\boldsymbol{\sigma}}_{CV}^N$  is not prescribed by the FFT-based scheme (evaluated as a post-treatment with eq. (3)), we solve the following set of

$3N_\phi$  equations for  $\mathcal{H}^0$ :

$$\underline{\boldsymbol{\sigma}}_i^N - \underline{\boldsymbol{\sigma}}_1^N = 0 \quad \forall i/2 \leq i \leq N_\phi \quad (14)$$

$$\sum_{i=1}^{N_\phi} f_i \underline{\boldsymbol{\epsilon}}_i^N - \underline{\boldsymbol{\epsilon}}_{CV}^N = 0 \quad (15)$$

In this case, the coefficients associated to the homogenization rule are the three components of the interface normal vector and the phases volume fractions  $\mathbf{C}_{CV} = \langle \mathbf{N}, \{f_i\}_{1 \leq i \leq N_\phi} \rangle$ .

### 2.3. Numerical resolution

Classically in non-linear mechanics codes, the constitutive relations (eq. (5)) are integrated with an incremental formulation at each time step, for a prescribed strain increment, to compute the stress increment. We denote by  $(\underline{\boldsymbol{\sigma}}_{CV}, \underline{\boldsymbol{\epsilon}}_{CV})$  and  $\Delta \underline{\boldsymbol{\sigma}}_{CV}, \Delta \underline{\boldsymbol{\epsilon}}_{CV}$  the initial (known) mechanical state and its incremental evolution over one time step for the CV, and  $(\underline{\boldsymbol{\sigma}}_i, \underline{\boldsymbol{\epsilon}}_i)$  and  $\Delta \underline{\boldsymbol{\sigma}}_i, \Delta \underline{\boldsymbol{\epsilon}}_i$  the corresponding local quantities for the phases contained within the CV. In this context, the local constitutive relations can be written:

$$\underline{\boldsymbol{\sigma}}_i + \Delta \underline{\boldsymbol{\sigma}}_i = \mathcal{F}_i(\underline{\boldsymbol{\sigma}}_i, \underline{\boldsymbol{\epsilon}}_i, \Delta \underline{\boldsymbol{\epsilon}}_i, \boldsymbol{\alpha}_i, \mathbf{C}_i) \quad \forall i/1 \leq i \leq N_\phi \quad (16)$$

The generic definition of a CV voxel model is given by eq. (7), which becomes, in this incremental context:

$$\mathcal{H}^0(\{\epsilon_i + \Delta \underline{\boldsymbol{\epsilon}}_i, \underline{\boldsymbol{\sigma}}_i\}_{1 \leq i \leq N_\phi}; \underline{\boldsymbol{\epsilon}}_{CV} + \Delta \underline{\boldsymbol{\epsilon}}_{CV}, \mathbf{C}_{CV}) = 0 \quad (17)$$

where  $\underline{\boldsymbol{\epsilon}}_{CV}, \Delta \underline{\boldsymbol{\epsilon}}_{CV}$  (prescribed by the FFT-based scheme) and the  $\{\epsilon_i, \underline{\boldsymbol{\sigma}}_i\}_{1 \leq i \leq N_\phi}$  are known, and the  $\{\Delta \underline{\boldsymbol{\epsilon}}_i\}_{1 \leq i \leq N_\phi}$  are unknown. In the following, to simplify the notation, we write eq. (17) omitting the dependance to the known quantities, which writes:

$$\mathcal{H}^0(\{\Delta \underline{\boldsymbol{\epsilon}}_i\}_{1 \leq i \leq N_\phi}) = 0 \quad (18)$$

Solving the problem requires then the resolution of the non-linear system of eq. (18). We chose to use iterative Newton-like methods to solve it. They consist in computing, at each iteration  $k$ :

$$\Delta \underline{\boldsymbol{\epsilon}}_i^k = \Delta \underline{\boldsymbol{\epsilon}}_i^{k-1} + \delta \Delta \underline{\boldsymbol{\epsilon}}_i^k \quad (19)$$

$$\mathcal{L}^k : \delta \Delta \underline{\boldsymbol{\epsilon}}_i^k = -\mathcal{H}^0\left(\{\Delta \underline{\boldsymbol{\epsilon}}_i^{k-1}\}_{1 \leq i \leq N_\phi}\right) \quad (20)$$

until eq. (18) is verified to the precision  $\eta$ :  $\mathcal{H}^0 \left( \left\{ \Delta \underline{\boldsymbol{\varepsilon}}_i^k \right\}_{1 \leq i \leq N_\phi} \right) < \eta$ . The choice of  $\mathcal{L}^k$  defines the iterative Newton-like method. In addition, Anderson's acceleration ((Anderson, 1965)) technique used for the FFT-based scheme fix-point algorithm is also applied using the pairs of solution/residual:

$$\left( \left\{ \Delta \underline{\boldsymbol{\varepsilon}}_i^k \right\}_{1 \leq i \leq N_\phi}, \mathcal{H}^0 \left( \left\{ \Delta \underline{\boldsymbol{\varepsilon}}_i^k \right\}_{1 \leq i \leq N_\phi} \right) \right)$$

We provide hereafter the specific description of the algorithm for laminate composite voxels only (eqs. (14) and (15)), as its formulation for Reuss and Voigt CV is almost identical. In incremental form, eq. (15) allows to write:

$$\Delta \underline{\boldsymbol{\varepsilon}}_1^N = \frac{1}{f_1} \left[ \Delta \underline{\boldsymbol{\varepsilon}}_{CV}^N - \sum_{i=2}^{N_\phi} f_i \Delta \underline{\boldsymbol{\varepsilon}}_i^N \right] \quad (21)$$

which can be introduced in eq. (14) to yield:

$$\mathcal{H}_i^0 = \underline{\boldsymbol{\sigma}}_{i+1}^N(\Delta \underline{\boldsymbol{\varepsilon}}_{i+1}^N) - \underline{\boldsymbol{\sigma}}_1^N \left( \frac{1}{f_1} \left[ \Delta \underline{\boldsymbol{\varepsilon}}_{CV}^N - \sum_{i=2}^{N_\phi} f_i \Delta \underline{\boldsymbol{\varepsilon}}_i^N \right] \right) \quad (22)$$

$$\forall i/1 \leq i \leq N_\phi - 1$$

It is a non-linear system of  $3(N_\phi - 1)$  equations, with a jacobian defined by:

$$d\mathcal{H}_{ij}^0 = \frac{\partial \mathcal{H}_i^0}{\partial \Delta \underline{\boldsymbol{\varepsilon}}_j^N} = \delta_{ij} \frac{\partial \Delta \underline{\boldsymbol{\sigma}}_{j+1}^N}{\partial \Delta \underline{\boldsymbol{\varepsilon}}_{j+1}^N} + \frac{f_{j+1}}{f_1} \frac{\partial \Delta \underline{\boldsymbol{\sigma}}_1^N}{\partial \Delta \underline{\boldsymbol{\varepsilon}}_1^N} \quad (23)$$

$$\forall (i, j)/1 \leq i \leq N_\phi - 1 ; 1 \leq j \leq N_\phi - 1$$

Numerically, the tensors  $\Delta \underline{\boldsymbol{\sigma}}_j^N$  and  $\Delta \underline{\boldsymbol{\varepsilon}}_j^N \forall j$  (that have only 3 independent components each) are handled as 3 components vectors, using Voigt notation. Hence, in this case,  $d\mathcal{H}_{ij}$  is a 3x3 matrix. The local tangent operator  $\frac{\partial \Delta \underline{\boldsymbol{\sigma}}_j^N}{\partial \Delta \underline{\boldsymbol{\varepsilon}}_j^N}$  is obtained by computing the 6x6 matrix  $\frac{\partial \Delta \underline{\boldsymbol{\sigma}}_j}{\partial \Delta \underline{\boldsymbol{\varepsilon}}_j}$  in the basis defined by  $\mathbf{N}$  and a unit vector tangent to the interface.

Three choices of tangent operator have been implemented for the laminate CV:

1.  $\mathcal{L}^{NR} = d\mathcal{H}^0$ , this choice is the Newton-Raphson method. In this case eq. (23) is explicitly computed from its analytical formula, for each component of the tangent operator.

2.  $\mathcal{L}^{num} = d\mathcal{H}^{num}$ , where  $d\mathcal{H}^{num}$  is a numerical approximation of  $d\mathcal{H}^0$ , computed as follow:

$$d\mathcal{H}_{ij}^{num} = \frac{\mathcal{H}_i^0(\dots, \Delta\boldsymbol{\underline{\epsilon}}_j^N + \epsilon, \dots) - \mathcal{H}_i^0(\dots, \Delta\boldsymbol{\underline{\epsilon}}_j^N, \dots)}{\epsilon} \quad (24)$$

where  $\epsilon$  is a perturbation that is small compared to  $\Delta\boldsymbol{\underline{\epsilon}}_j$  ( $\epsilon \approx 10^{-8}$  is used in the following). This choice is a numerical approximation of the Newton-Raphson method.

3.  $\mathcal{L}^0$ , the constant isotropic linear elastic tangent operator corresponding to a Quasi-Newton method. Its components are computed as follows:

$$\mathcal{L}_{ij} = \delta_{ij} \underline{\underline{\mathbf{A}}}_N^{j+1} + \frac{f_{j+1}}{f_1} \underline{\underline{\mathbf{A}}}_N^1 \quad (25)$$

$$\forall (i, j) / 1 \leq i, j \leq N_\phi - 1$$

where  $\underline{\underline{\mathbf{A}}}_N^j$  are the equivalent elastic moduli tensors of the constitutive phases of the CV restricted to the normal components of the tensors, as detailed above for the true tangent operator.

Note that for Reuss CV, only the Quasi-Newton method has been implemented, and that for Voigt CV, no iterative resolution is needed. In the following, laminate CV equations will always be integrated with the Newton-Raphson method. No distinction between this algorithm (with  $\mathcal{L}^{NR}$ ) and its numerical approximation (with  $\mathcal{L}^{num}$ ) will be done as they have no incidence on the results. Simply note that using  $\mathcal{L}^{num}$  comes with an additional computational cost as it requires  $N_\phi - 1$  evaluations of  $\mathcal{H}^0(\dots, \Delta\boldsymbol{\underline{\epsilon}}_j^N + \epsilon, \dots)$  ( $\forall j \ 2 \leq j \leq N_\phi$ ). In addition, note that the convergence acceleration technique is systematically applied, every three iterations, for all three algorithms.

This formulation is generic and thus can be used with any type of constitutive equations for the phases of the composite voxels. In addition, the use of a numerically evaluated jacobian or a constant tangent operator allows to use non-linear behaviors without knowing the exact tangent operator of the constitutive equations  $\frac{\partial \Delta \boldsymbol{\underline{\sigma}}}{\partial \Delta \boldsymbol{\underline{\epsilon}}}$ .

### 3. Material

#### 3.1. Explicit slip band modeling

Similarly to [Zhang et al. \(2010\)](#), we consider in a polycrystalline unit cell, a distribution of equally spaced bands of constant width that are parallel to

the slip systems of each grain. As a first step, we consider in this paper a single slip plane per grain, with normal direction  $\mathbf{n}$ . The band width is noted  $\omega_b$ , the band spacing  $d_b$ , the mean grain size  $d_g$  and the voxel size  $\delta x$ . As a result, the average number of bands per grain is  $N_b = \frac{d_g}{d_b}$  and the average band volume fraction is  $f_b = \frac{\omega_b}{d_b}$ .

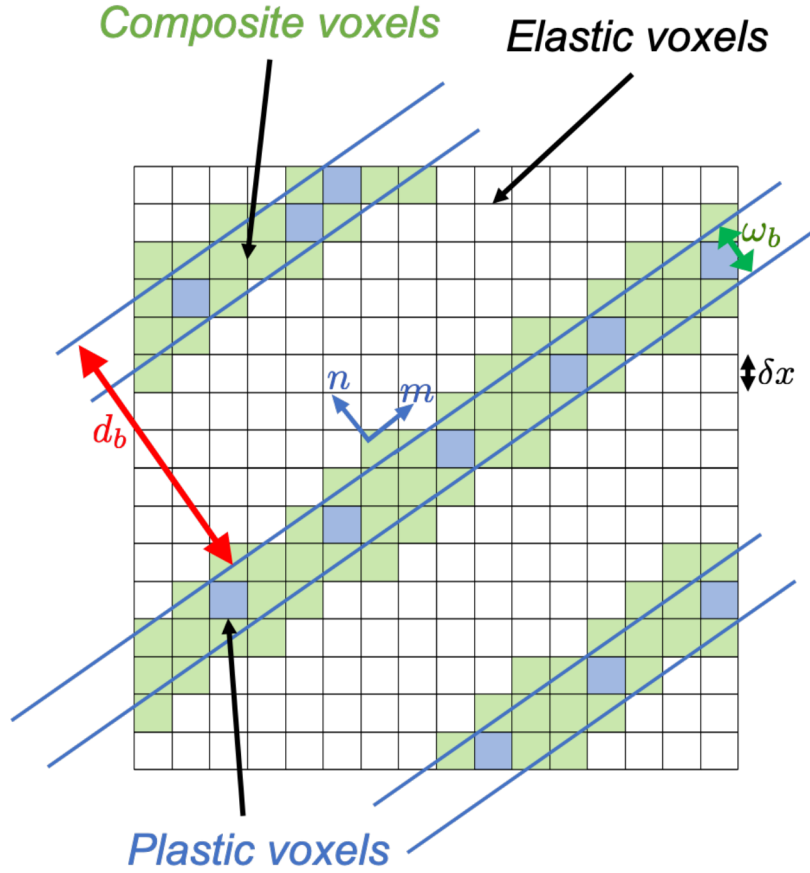


Figure 1: Planar representation of potential slip bands of fixed width  $\omega_b$  and spacing  $d_b$  on a regular grid with homogeneous and composite voxels, for a single slip system defined by its glide and normal to slip plane directions  $\mathbf{m}$  and  $\mathbf{n}$ .

As shown on the planar schematic of [fig. 1](#), each potential slip band is defined by 2 planes crossing the discretization grid, with normal direction  $\mathbf{n}$ . For each voxel, the intersection points with the voxel edges are computed.

When no intersection is found: each voxel lying entirely between the two planes, is given a plastic behavior, and each voxel lying entirely outside is given an isotropic linear elastic behavior. Each voxel crossed by one of these planes is defined as a composite voxel composed of the plastic and the elastic phase. For each plane, the volume of the region bounded by the intersection points of the voxel edges and the voxel vertices located on the same side of the plane in the direction  $\mathbf{n}$  is computed with the Convex Hull function (*convhull*) of the Octave software. This way, the volume fraction of each phase can be computed. Complemented with the three components of  $\mathbf{n}$ , all the microstructural informations needed to use the three different CV models proposed in [section 2](#) are obtained.

In this study, only unit cells with a single slip plane per grain have been generated. In fact, generating sets of parallel slip bands with different orientations requires to handle the definition of CV, which remains an open question for future work. Furthermore, this framework is already sufficient to study materials with a slip behavior dominated by a single slip plane, as for instance irradiated textured Zr alloys under specific loading (see [section 3.3](#)).

### 3.2. Crystallographic texture

This paper aims also at showing the potential of explicit slip band modeling for the prediction of the consequences of slip localization on grain boundary normal stresses or kinematic hardening due to plastic strain incompatibilities. Polycrystalline texture can have a significant impact on this quantities as a strong texture will favor slip transmission at grain boundaries, which should result in lower stress concentrations than intense slip bands intersecting ending up on underformed grains. Hence, it has been accounted for in our idealized material of irradiated Zr alloys with a realistic crystallographic texture for Zr alloy cladding tubes.

The texture of cold-rolled recrystallized Zr alloys used for cladding tubes has been studied experimentally by [Pawlik \(1986\)](#) and consists in a majority of grains having their  $\langle c \rangle$  axis at an angle  $\pm 30^\circ$  of the radial direction of the tubes, in the plane defined by the radial direction and the transverse direction (TD). This plane is orthogonal to the rolling direction (RD), corresponding to the tube axis.

A representative orientation distribution density function has been built and used to generate a file of  $1 \times 10^5$  grain orientations that is representative of the texture. In order to generate representative polycrystalline unit cells of this material, random sets of orientations are drawn from this file. To

ensure that a set of orientations is a good approximation of the reference texture with  $10^5$  grains, the Kearns anisotropy factor is used (Fong (2013); Kearns (1965)). For a given direction  $\mathbf{d}$ , denoting by  $\theta_i$  the angle between the  $\langle c \rangle$  axis of each grain with  $\mathbf{d}$ , the Kearns factor  $K_d$  of  $\langle c \rangle$  axis in direction  $\mathbf{d}$  is given by:

$$K_d = \sum_i f_i \cos^2(\theta_i) \quad (26)$$

where the  $f_i$  are the volume fraction of each grain with respect to the aggregate.

For each orientation set drawn from the reference file, the Kearns factors for the three directions of the cartesian basis  $\mathbf{e}_1, \mathbf{e}_2, \mathbf{e}_3$ , for the  $\langle c \rangle$  axis are computed, and compared to the factors of the  $1 \times 10^5$  grains texture. If the relative distance in quadratic norm of the vectors containing the 3 factors is higher than 0.1%, the orientation set is rejected and a new one is drawn. This procedure allows to have small orientation sets that are more representative of the anisotropy of the considered material, as shown on fig. 2.

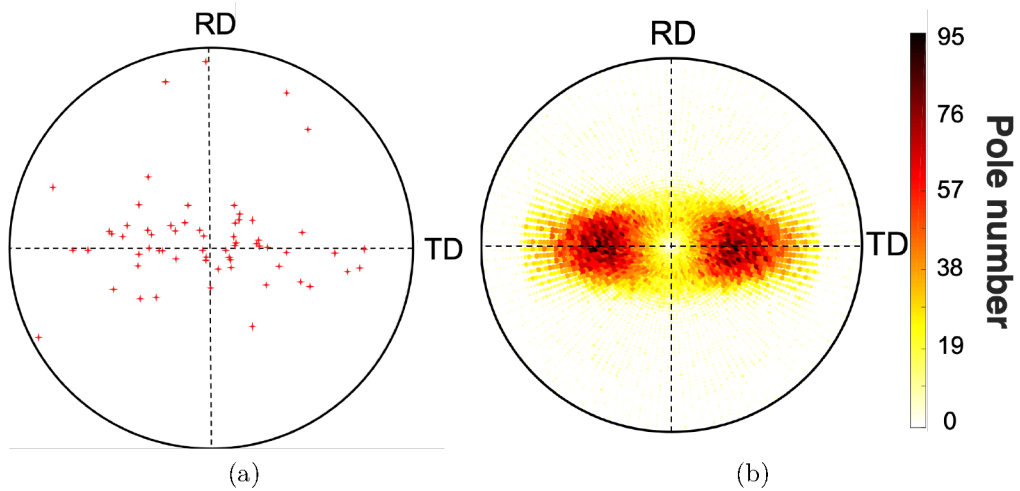


Figure 2:  $\langle c \rangle$  axis pole figure obtained for a random set of 64 grains texture (a) with equivalent Kearns factors than the reference texture for 100000 grains (b). TD: transverse direction, RD: rolling direction

### 3.3. Unit cells and slip localization modeling

As shown by observations (Onchi et al. (1977); Onimus et al. (2012, 2004)), irradiated Zr alloys strained along the TD mainly deform through

basal channeling. Thus, as a first approximation, only basal slip is accounted for in the simulations. For each unit cell, a polycrystalline microstructure is generated with a prescribed number of grains and grid resolution with a Voronoi tessellation. Then a random set of orientation representative of the texture is chosen according to the procedure described in [section 3.2](#), attributing the normal vector to the basal plane to each grain of the Voronoi tessellation. Finally, after choosing the width and spacing of slip bands, the band pattern is generated within each grain along with composite voxels.

Two types of potential slip band patterns have been generated within a 64 grains polycrystalline aggregate with a representative texture. First, a set of pattern with a fixed potential slip band volume fraction (20%) and varying number of bands is generated. When reducing the number of slip bands per grain, band width rises as well as band spacing. This set of patterns allows to isolate the effect of the repartition of the slip bands constituting the plastic phase from the effect of a varying plastic phase volume fraction, and thus evidences the pure effect of slip localization. A second set of patterns is generated with an increasing number of bands of fixed width,  $\frac{\omega_b}{d_g} = \frac{1}{100}$ , which is the typical order of the ratio between grain size ( $\sim 5 \mu\text{m}$  to  $10 \mu\text{m}$ ) and clear channel width ( $\sim 40 \text{ nm}$  to  $100 \text{ nm}$ ) observed in irradiated Zr alloys. Two examples are shown on [fig. 3](#). Hence, the intensity of slip localization in this study is varied essentially by changing the slip band spacing: the lower the band spacing, the lower the intensity of localization.

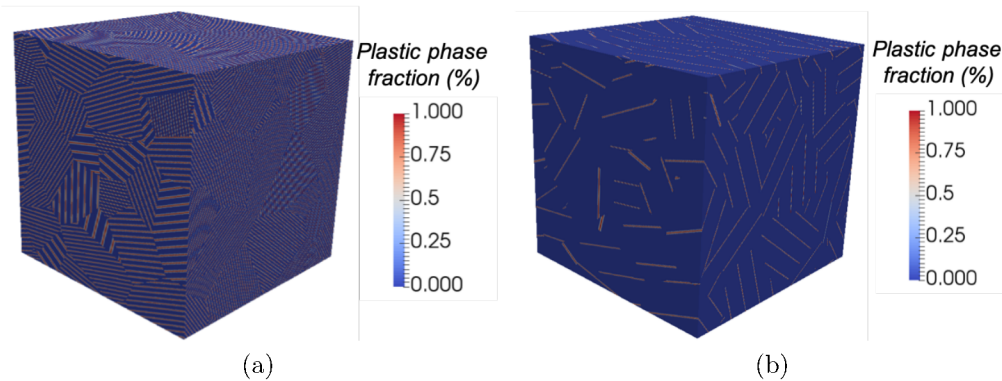


Figure 3: 64 grains polycrystalline unit cells ( $400^3 = 64$  million voxels) with different number of potential basal slip bands with Zr cladding tubes texture. Bands width is of the order of basal clear channels width in irradiated Zirconium alloys:  $\frac{\omega_b}{d_g} = \frac{1}{100}$ .

### 3.4. Mechanical behavior

The constitutive modeling chosen for the plastic phase is an almost perfectly plastic crystal plasticity model with a Norton flow rule, summarized by eqs. (27) to (31):

$$\underline{\boldsymbol{\varepsilon}} = \underline{\boldsymbol{\varepsilon}}^e + \underline{\boldsymbol{\varepsilon}}^p \quad (27)$$

$$\underline{\boldsymbol{\sigma}} = \underline{\boldsymbol{\Lambda}} : \underline{\boldsymbol{\varepsilon}}^e \quad (28)$$

$$\underline{\boldsymbol{\varepsilon}}^p = \sum_{s=1}^N \gamma^s \underline{\boldsymbol{\mu}}^s \quad (29)$$

$$\dot{\gamma}^s = \text{sign}(\tau^s) \left\langle \frac{|\tau^s| - \tau_c}{K} \right\rangle^n \quad (30)$$

$$\tau^s = \underline{\boldsymbol{\sigma}} : \underline{\boldsymbol{\mu}}^s \quad (31)$$

where  $\underline{\boldsymbol{\varepsilon}}^e$  and  $\underline{\boldsymbol{\varepsilon}}^p$  are respectively the elastic and plastic strain tensors, where  $\underline{\boldsymbol{\Lambda}}$  is the elastic moduli tensor,  $\gamma^s$ ,  $\dot{\gamma}^s$  and  $\tau^s$  are respectively the plastic slip, plastic slip rate and resolved shear stress for the slip system  $s$ , and  $\underline{\boldsymbol{\mu}}^s = \frac{1}{2}(\mathbf{m}^s \otimes \mathbf{n}^s + \mathbf{n}^s \otimes \mathbf{m}^s)$  is the symmetric Schmid tensor of slip system  $s$ , with  $\mathbf{m}^s$  and  $\mathbf{n}^s$  its slip direction and normal to slip plane direction.

The critical resolved shear stress  $\tau_c = 80$  MPa (after [Onimus and Bechade \(2009\)](#)) is constant and the Norton flow rule coefficients  $n = 20$  and  $K = 10$  MPa s<sup>1/n</sup> are chosen so that the behavior is almost rate-independent. This choice has been made to avoid any variation of the macroscopic stress linked to local hardening or softening terms, and thus isolate the effect of the distribution of slip bands on the macroscopical kinematic hardening. This strong simplification amounts to considering potential slip bands as clear channels completely depleted from irradiation induced defects at incipient plasticity. The transversely isotropic elasticity of Zr alloys is accounted for in the elasticity tensor. It is defined by the following elastic moduli:

- $E_a = 70\,028$  MPa is the Young modulus along directions  $\langle a \rangle$  and  $E_c = 110\,354$  MPa along direction  $\langle c \rangle$
- $G_a = 22\,900$  MPa is the shear modulus in basal plane and  $G_{ac} = 27\,000$  MPa in  $(\langle a \rangle, \langle c \rangle)$  planes
- $\nu_a = 0.203$  is the Poisson coefficient in basal plane and  $\nu_{ac} = 0.529$  in  $(\langle a \rangle, \langle c \rangle)$  planes

Outside of the slip bands, the material, as mentioned earlier, is purely elastic, with the same elastic moduli. In practice, these relations are implemented in a UMAT subroutine using the Mfront code generator (Helfer et al. (2015)) and solved with an implicit Newton-Raphson method. This implementation allows to compute easily the local tangent operator of the constitutive relation  $\frac{\partial \Delta \boldsymbol{\sigma}}{\partial \Delta \boldsymbol{\varepsilon}}$  of each material phase of the composite voxels. It is used to apply the Newton-Raphson method for the resolution of laminate CV models.

## 4. Results

### 4.1. Enhanced computational efficiency induced by composite voxels

We first investigate the impact of composite voxels on the computational cost of polycrystalline simulations with explicit slip bands. Out of simplicity, for this set of simulations, unit cells are generated with an isotropic texture, the material elasticity is chosen isotropic linear with Young's modulus  $E = 1 \times 10^5$  MPa and Poisson's ratio  $\nu = 0.3$ , and the critical resolved shear stress is set to  $\tau_c = 100$  MPa.

The grid resolution is defined as the ratio between the band width and the voxel size  $r = \frac{\omega_b}{\delta x}$ . The simulations are carried out for increasing resolution verifying  $r^P = 2^P \cdot r^0$ , where  $P$  is the grid refinement coefficient, and  $r^0$  is the initial resolution. 27 grains unit cells are generated with two sets of band patterns: one with  $\frac{\omega_b}{d_g} = \frac{1}{10}$  and  $r^0 = 1$  ( $P = 1, 2, 4, 8, 16$  i.e.  $30^3, 60^3, 120^3, 240^3, 480^3$  voxels), and another with  $\frac{\omega_b}{d_g} = \frac{1}{50}$  and  $r^0 = 0.5$  ( $P = 1, 2, 4, 8$  i.e.  $75^3, 150^3, 300^3, 600^3$  voxels), where  $d_g$  is the mean grain size in the polycrystal. The first pattern allows to study the convergence with resolution up to high number of voxels per band and the second is used to study the convergence when modeling thin bands.

The unit cell is submitted to a mean tensile strain loading in the direction  $\mathbf{e}_3$  up to  $\underline{\varepsilon}_{33} = 0.01$ , where  $\mathbf{e}_1, \mathbf{e}_2, \mathbf{e}_3$  is the cartesian basis. All other components of the mean stress tensor are prescribed to zero. The simulation is carried out with strain increments of  $10^{-5}$ , at a strain rate of  $1 \times 10^{-5} \text{ s}^{-1}$ . Figure 4 shows a comparison of the stress-strain curves obtained without CV and with laminate CV (Reuss and Voigt CV have been omitted for readability) for all resolutions of the first pattern ( $\frac{\omega_b}{d_g} = \frac{1}{10}$ ). It shows that the model relying on laminate CV converge to the same solution than classical FFT scheme, and that it converges faster.

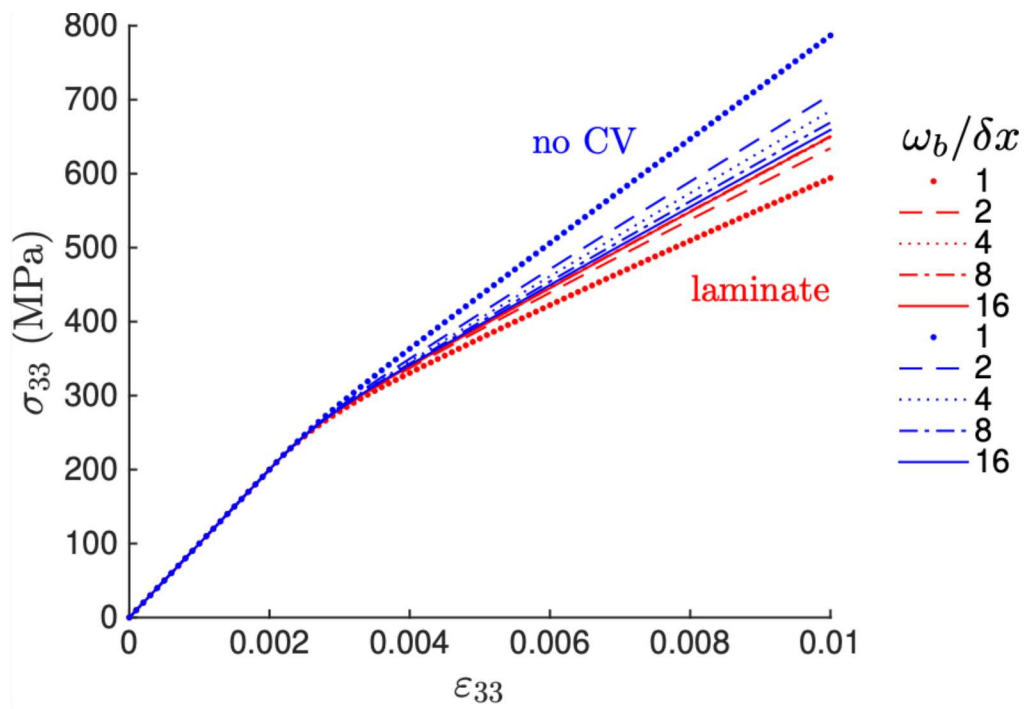


Figure 4: Simulated stress-strain curve without composite voxels and with laminar composite voxels for a 27 grains polycrystal with 3 bands per grain in average ( $\frac{\omega_b}{d_g} = \frac{1}{10}$ ) for increasing grid resolution.

To quantify the convergence improvement, three CV models presented in [section 2.2](#) are compared to the classical FFT scheme. The convergence of  $\underline{\sigma}_f = \underline{\sigma}_{33}(\underline{\epsilon}_{33} = 0.01)$  is studied. Two error indicators are used to quantify its evolution with grid refinement:

$$E_{cv}(P) = \frac{\underline{\sigma}_f(P) - \underline{\sigma}_f(P-1)}{\underline{\sigma}_f(P-1)} \quad (32)$$

$$E_{rel}\left(\frac{\omega_b}{\delta x}, \underline{\sigma}^{ref}\right) = \frac{\underline{\sigma}_f\left(\frac{\omega_b}{\delta x}\right) - \underline{\sigma}^{ref}}{\underline{\sigma}^{ref}} \quad (33)$$

A low value of  $E_{cv}(K)$ , the convergence error, indicates that the solution is converged with respect to grid resolution and  $E_{rel}$ , the relative error, evaluates the precision of a given simulation with respect to a reference value obtained with laminate CV at the highest resolution.

[Figure 5](#)-(a-b) presents the evolution of  $E_{cv}$  with grid refinement for the two patterns. It shows that laminate CV yield the best convergence rate in both cases, and convergence is even faster when modeling thin bands (b). With the other CV models  $E_{cv}$  convergence is slower, as well as without CV, but Voigt CV yield an even worse convergence rate. Reuss CV convergence rate is better, but simulations could not converge unless  $\frac{\omega_b}{\delta x} \geq 4$ , and only for strain increments of  $10^{-6}$  resulting in much longer simulations than all other models. This could be attributed to the use of the quasi-Newton method instead of Newton-Raphson method. However, laminate CV simulation were successfully conducted with the Quasi-Newton method, indicating that Reuss CV model is more difficult to solve in this case.

The convergence error is below  $10^{-3}$  for the highest grid resolution value with laminate CV, justifying the choice of this case as the reference value to compute the relative error  $E_{rel}$ .

The evolution of the relative error with computational time is shown on [fig. 5](#)-(c). It shows that the use of laminate CV allows to reduce the computational time from one to two orders of magnitude to obtain a precision lower than 2% when compared to the simulations without CV voxels. In other words, to get the same precision than without CV with a resolution 4 to 8 times lower ( 64 to 512 times less voxels). With  $\frac{\omega_b}{\delta x} = 1$ , the relative error is  $\sim 1\%$  with laminate CV for thin bands ( $\frac{\omega_b}{d_g} = \frac{1}{50}$ ) as illustrated on [fig. 5](#)-(d). The provided computational times have been obtained on 1000 cores (

2.4 GHz and 4.6 Go RAM per core) on the supercomputer [Cobalt<sup>2</sup>](#).

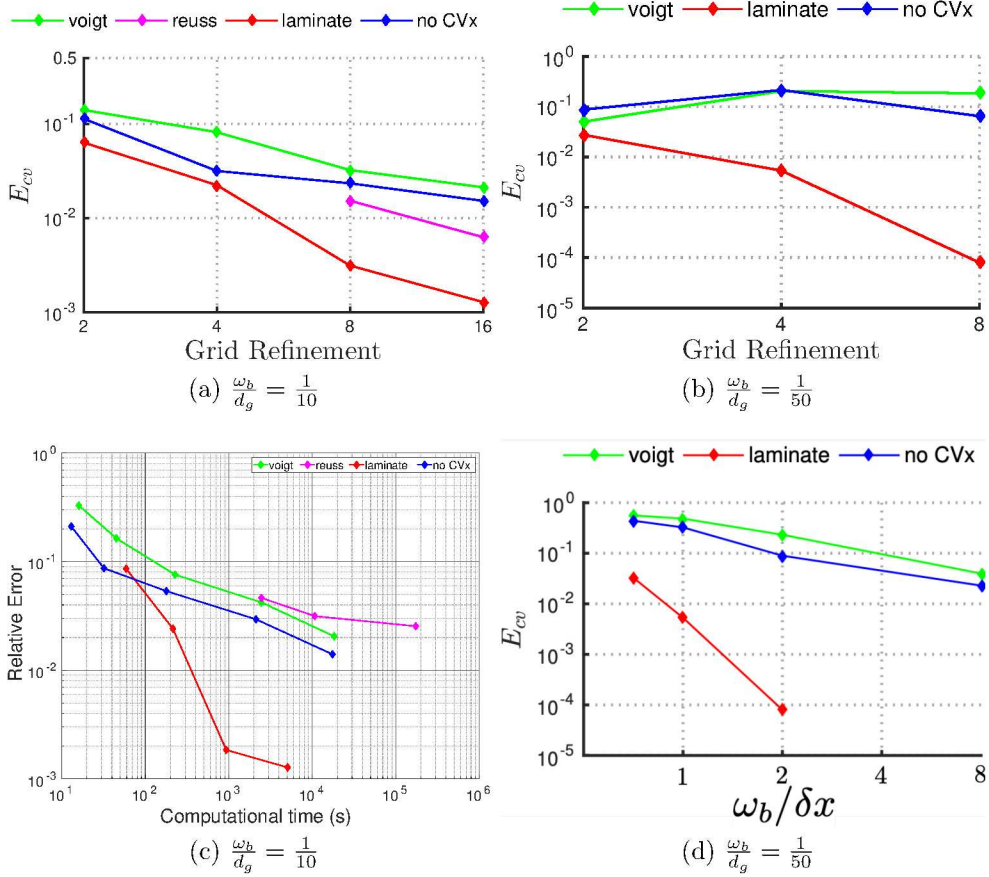


Figure 5: Evolution of convergence error with grid refinement (a-b). Evolution of the relative error with respect to the reference with computational time (c) and with the number of voxels per slip band  $\omega_b/\delta x$ . The relative error reference is the unit cell with highest grid resolution with laminate CV for each band pattern ( $480^3$  voxels for (c) and  $600^3$  for (d)). From left to right the points correspond for each curve to the following number of voxels: for (c)  $30^3, 60^3, 120^3, 240^3, 480^3$ , for (d)  $75^3, 150^3, 300^3, 600^3$ . All simulations with Reuss CV and  $\frac{\omega_b}{\delta x} < 4$  have not converged and are not plotted.

These results demonstrate that laminate CV strongly enhance the efficiency of explicit slip band modeling. The gain is even higher for thin slip

<sup>2</sup>[http://www-ccrt.cea.fr/fr/moyen\\_de\\_calcul/index.htm](http://www-ccrt.cea.fr/fr/moyen_de_calcul/index.htm)

bands compared to the grain size, which is of prime interest for the modeling of clear channels in irradiated metals. On the other hand, Reuss and Voigt CV deteriorate the efficiency compared to a modeling without CV.

#### 4.2. Increased kinematic hardening induced by slip localization

Here, we investigate the ability of explicit slip band modeling to predict the influence of strain localization on the mechanical behavior of irradiated metals. In particular, we study the ability of this modeling approach to reproduce the increased Bauschinger effect observed in irradiated Zr arising from plastic strain incompatibilities generated by clear channels formation.

64 grains unit cells of the idealized material described in [section 3](#) are generated with a set of band patterns with an increasing number of bands per grain of fixed width,  $\frac{\omega_b}{d_g} = \frac{1}{100}$ , which is consistent with the ratio between grain size ( $\sim 5 \mu\text{m}$  to  $10 \mu\text{m}$ ) and clear channel width ( $\sim 40 \text{ nm}$  to  $100 \text{ nm}$ ) observed in irradiated Zr alloys. Hence, the band volume fraction in % is directly equal to the mean number of bands per grain. The degree of strain localization increases with band spacing (with decreasing bands number).

Grid resolution is set to  $400^3$  voxels, in order to have  $\frac{\omega_b}{\delta x} = 1$ , for which laminate CV yield a precision of the order of 1% (see [section 4.1](#)). Thus all simulations presented below involve 64 millions voxels, and laminate CV are systematically used. Unit cells are submitted to a tension-compression loading in TD up to 1% strain, with strain increments of  $10^{-5}$ , at a strain rate of  $1 \times 10^{-5} \text{ s}^{-1}$ .

As the behavior is almost perfectly plastic, only kinematic hardening due to plastic strain incompatibilities that must be elastically accommodated is predicted by this model. [Figure 6](#) shows the stress-strain curves (a-b) obtained with the different band patterns and the evolution of the isotropic ( $R$ ) and kinematic ( $X$ ) hardening (c-d), computed at 1% strain, as a function of the bands volume fraction. It confirms that no isotropic hardening is predicted. It reveals a strong increase in kinematic hardening when the number of bands is decreasing, i.e. when slip localization increases. With 3 potential slip bands per grain in average, which is close to the average number of clear channels observed in irradiated Zr alloys ([Onimus et al. \(2004\)](#)), the hardening is  $\sim 60\%$  higher than for the 100% plastic polycrystal. [Figure 6-\(d\)](#) shows the evolution of hardening components for the second set of patterns, with fixed bands volume fraction. Again, strain localization increases kinematic hardening showing that this effect is not purely associated

with the variation of bands volume fraction in the first case (a) but also to the spatial distribution of slip bands.

In conclusion, this modeling approach predicts a strong increase of kinematic hardening for increased slip localization, understood as the increase of slip band spacing, which is qualitatively consistent with the stronger Bauschinger effect observed on irradiated textured Zr alloys compared to for non irradiated ones.

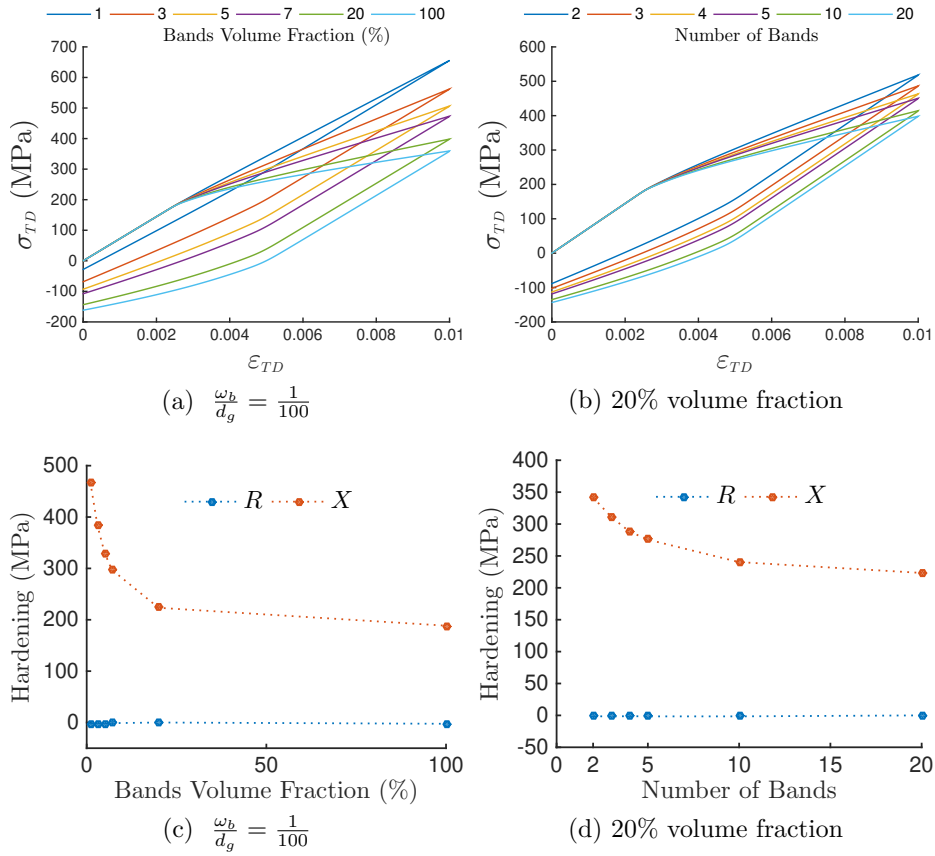


Figure 6: (a): Stress-strain curves (a-b) for a loading-unloading tensile test ( $\pm 1\%$  strain in  $TD$ ) and evolution of Kinematic and Isotropic hardening values (c-d) for various band volume fractions with fixed band width:  $\frac{\omega_b}{d_g} = \frac{1}{100}$ . (a & c) and for various band number per grain with fixed 20% volume fraction (b & d)

#### 4.3. Grain boundary stress concentrations induced by slip localization

We study here the predicted evolution of the grain boundary normal stress distribution with increasing slip localization. If this question is not really relevant for Zr alloys, these quantities are thought to be a good indicator to build an intergranular crack initiation criterion for the prediction of IASCC observed in irradiated stainless steels.

The stress fields computed at 1% tensile strain with the previously described simulations have been post-processed in order to compute the grain boundary normal stress distribution. The Voronoi tessellation used to generate the polycrystalline unit cell provides the exact definition of the planes forming the grain facets: their position and their normal vector  $\mathbf{N}_i$ . From this information, grain boundary voxels lying on each facet can be detected, and the grain boundary normal stress is evaluated by computing  $\mathbf{N}_i \cdot \underline{\boldsymbol{\sigma}} \cdot \mathbf{N}_i$ . In addition,  $\underline{\boldsymbol{\sigma}}_{95\%}$ , the 95th grain boundary normal stress percentile is computed from the distribution, as the upper tail is the relevant part of the curve used to build intergranular cracking criterions (Hure et al. (2016)).

Figure 7 shows the evolution of the grain boundary normal stress distribution and  $\underline{\boldsymbol{\sigma}}_{95\%}$  for the set of patterns representative of basal clear channel width ( $\frac{\omega_b}{d_g} = \frac{1}{100}$ ). It reveals (a) that when increasing slip localization, the grain boundary normal stress distribution becomes less symmetric and spreads towards the high tensile stress values. This is confirmed by the evolution of  $\underline{\boldsymbol{\sigma}}_{95\%}$  (b), that increases when reducing the number of bands.

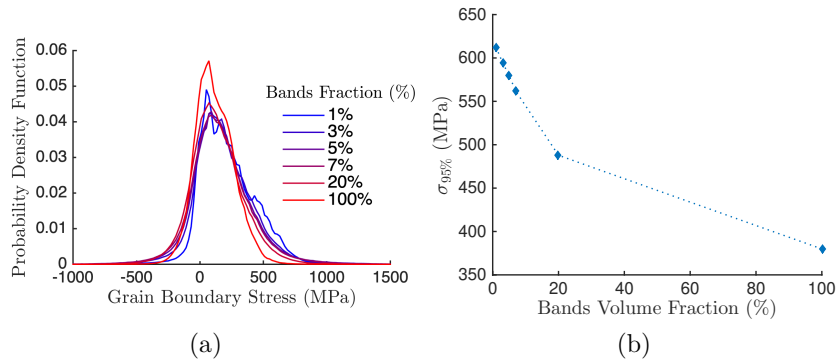


Figure 7: Grain boundary stress distribution at 1% tensile strain in *TD* (a) and evolution of its 95<sup>th</sup> percentile (b) for various band volume fractions with fixed band width:  $\frac{\omega_b}{d_g} = \frac{1}{100}$ .

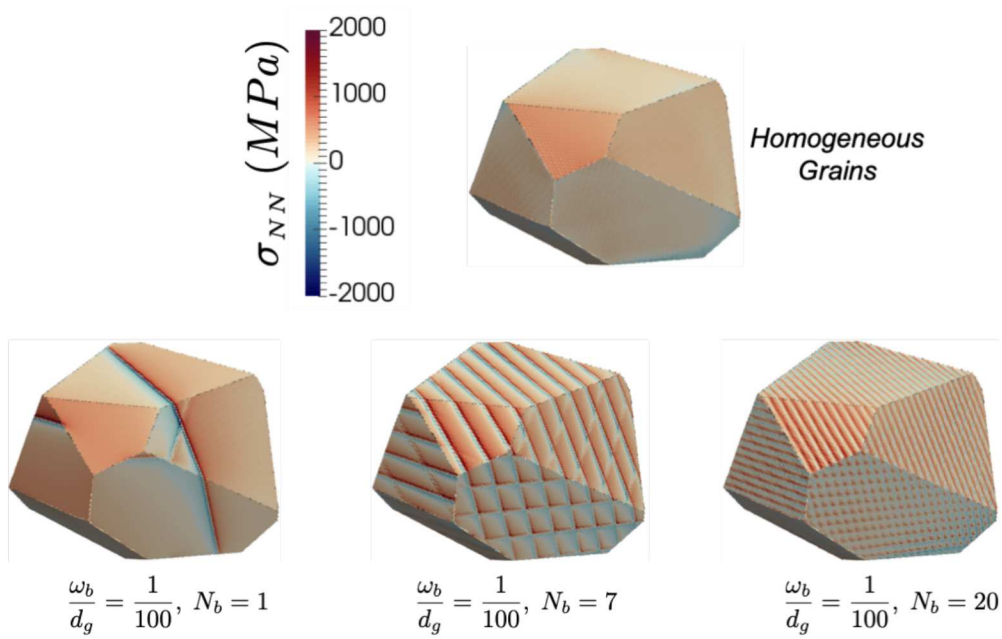


Figure 8: Grain boundary normal stress fields on a grain, for various band width  $\omega_b$  and number of bands  $N_b$ . (64 grains polycrystal with in all cases:  $\frac{d_g}{\delta x} = \frac{1}{100}$  i.e. 64 millions voxels)

Figure 8 presents the associated normal stress fields on the surface of a grain of the polycrystalline microstructure, for various slip band patterns. Clear stress concentration corresponding at slip band tips can be observed in all cases, except for the homogeneous grains case. Normal stress concentrations are stronger when the degree of localization is higher (i.e. with a lower number of bands), which is consistent with the results presented on fig. 7.

These results highlight the ability of this modeling approach to predict increased stress concentrations on grain boundaries induced by slip localization, and thus help to develop numerical strategies devoted to predict intergranular fracture in irradiated metals.

## 5. Discussion

### 5.1. Stress concentrations and kinematic hardening

As evidenced by these results, accounting explicitly for localized slip predicts a strong Bauschinger effect when prescribing a low number of potential slip bands per grain. Our simulations show ( fig. 9-b) that intersections between active slip bands and grain boundaries are associated to important local stress concentrations due to the strong plastic strain incompatibility between the non deforming grain and the intense shear in the slip band on both sides of the grain boundary. These stress concentrations are most certainly the cause of the increased kinematic hardening.

The role of plastic strain incompatibilities is highlighted by contrast with the absence of stress concentrations observed in the areas circled in purple on the equivalent strain and stress fields shown on fig. 9-(a-b). They reveal important slip transmission on two boundaries of the same grain that induce almost no stress concentrations. It is remarkable that the orientation of the slip bands involved at these boundaries differs only from a small angle and that the strain in the bands seems continuous at the boundary. This features will generate indeed little incompatibilities and thus will not induce stress concentrations. Note that this configuration, considering the small number of grains modeled in the unit cell, is most likely due to the consideration of the texture in the modeling, demonstrating that this type of models could help gain insight into texture effects on the local mechanical behavior of polycrystals.

These simulations qualitatively reproduce the mechanism proposed by Luft (1991) and Onimus and Bechade (2009), that explain the increased

Bauschinger effect in irradiated Zr alloys by the strong strain incompatibilities induced by basal clear channels on the neighboring non deforming grains. However, it is surely overestimated as prismatic or pyramidal slip systems could be activated by the strong stresses at channel/grain boundary intersections and help accommodate incompatibilities, reducing the induced kinematic hardening. Likewise, modeling other slip plane families to account for prismatic or pyramidal channeling could potentially strongly affect the increased kinematic hardening.

Moreover, it is interesting to note that this increased kinematic hardening is obtained without any changes of the material parameters describing the behavior of the plastic phase, and even without changing its volume fraction. This type of approach could then lead to reconsider the value of local kinematic hardening coefficients used in crystal plasticity models when identifying them using full-field simulations.

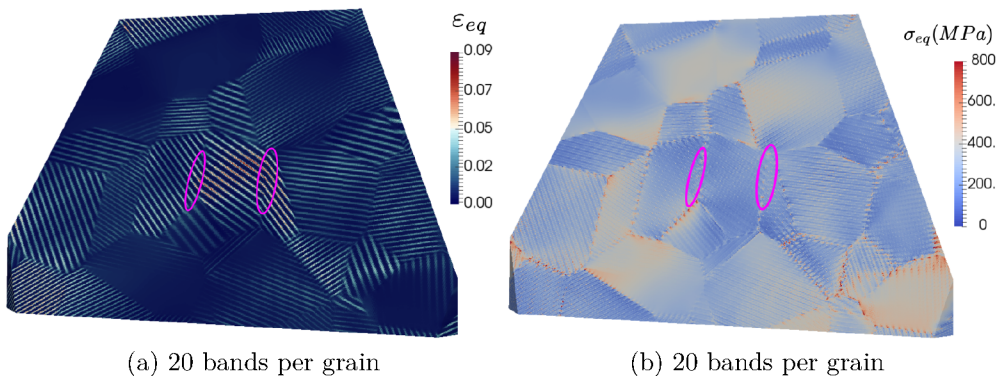


Figure 9: Internal sections of equivalent strain (a) and equivalent stress (b) fields with 20 potential slip bands per grain in average, extracted from 64 grain polycrystal simulations at 1% tensile strain in *TD* (64 millions voxels). Purple circles indicate regions where slip bands of different grains intersect at the grain boundary.

## 5.2. Mesh dependance

The observation of the simulated Von Mises equivalent strain fields reveals that when the number of voxels inside slip bands becomes larger than 4, deformation tends to localize on the band boundaries, which is not consistent with physical slip bands that have a rather homogeneous aspect along their width (as do clear channels). This is illustrated on [fig. 10-\(a\)](#). This artifact

is most likely due to the plastic instability inherent to the quasi-perfectly plastic behavior, and could be even more pronounced when using a softening behavior in slip bands. Fortunately, as shown in section 4.1, laminate CV allow to obtain an accurate solution for  $1 \leq \frac{\omega_b}{\delta x} \leq 4$  (error is below 1% in all cases with 2 voxels in the band width) as well as smooth deformation fields inside the bands as shown on figure fig. 9-(a). Hence, this artifact could become problematic only when simulating slip bands of a width close to the grain size, for which using less than 4 voxels per band width would become too coarse. In practice, the relevant width of physical slip bands is much lower than this.

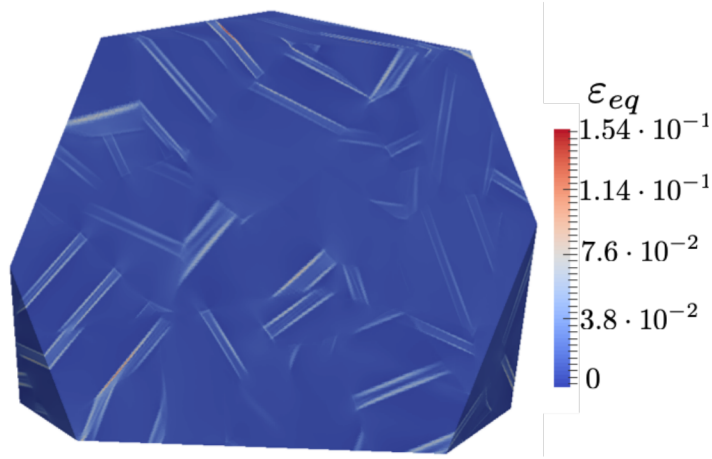


Figure 10: Internal section of the equivalent strain field at 1% tensile strain in  $TD$  for a 64 grains polycrystal with 20% slip band volume fraction and 2 bands per grain in average:  $\frac{\omega_b}{d_g} = \frac{1}{10}$ ,  $\frac{\omega_b}{\delta x} = 10$  (64 millions voxels)

### 5.3. Computational time

The simulations carried out on our model material (sections 4.2 and 4.3) have required 1 to 6 hours of calculation for each on the Cobalt<sup>3</sup> supercomputer with 4000 cores ( 2.4GHz and 4.6 Go RAM per core). Note that when using more usual computational resources the computational time on 100-200 cores would have been comprised between one and five days,

<sup>3</sup>[http://www-ccrt.cea.fr/fr/moyen\\_de\\_calcul/index.htm](http://www-ccrt.cea.fr/fr/moyen_de_calcul/index.htm)

which remains reasonable. Overall, this demonstrates that a parallel implementation is mandatory to achieve such simulations. Besides, the results of [section 4.1](#) show that with a standard FFT-based solver (without CV), the computational cost to conduct this study would have been 1 or 2 order or magnitude higher, which represents weeks for a single computation on standard resources. Hence, the use of laminate CV together with a parallel implementation appears mandatory to use explicit slip band modeling in three dimensional realistic polycrystalline simulations.

#### *5.4. Representativity of the results*

Finally, it must be mentioned that the results presented here have been obtained for only one randomly generated polycrystalline aggregate and texture. They provide an interesting qualitative insight into the possibilities opened by this modeling approach, they are certainly not statistically representative of the behavior of our model material and the magnitude of the simulated increase in kinematic hardening could change significantly when increasing the unit cell size. Assessing this representativity should be mandatory for future studies aiming at obtaining quantitatively representative results.

Yet, the ambition of this study was only to demonstrate that explicit modeling of clear channels was a valid tool to simulate the strain localization induced stress concentrations. We believe that the magnitude of the variation of the kinematic hardening with the number of bands per grain, and the observed strong stress concentration and grain boundary normal stress fields evidenced by our study are a strong enough evidence of the interest of this modeling approach.

## **6. Conclusions and future prospects**

We proposed a generic and unified formulation of composite voxel models in the context of small strains, allowing to define composite voxels with any arbitrary number of phases with any linear or non-linear constitutive relations. It has been used to implement three types of generic composite voxel models within the massively FFT-based solver AMITEX\_FFTP: Voigt, Reuss and Laminate composite voxels. We applied these to reduce the computational cost of explicit slip band modeling. It has been shown that laminate composite voxels allows to reduce the computational cost of such simulations, reducing the needed resolution to obtain a precise solution by a factor  $4^3$  to

$8^3$ , resulting in a reduction of computational time of one to two orders of magnitude and a reduced memory needed for the simulations. Moreover, we have shown that this numerical framework is mandatory to conduct, within a reasonable time, 3D realistic polycrystalline simulations with explicit slip bands, using conventional parallel computers.

We demonstrated that this approach can be used to simulate the impact of basal channeling in irradiated textured Zr alloys. The increased localized slip induced by irradiation is explicitly accounted for by increasing slip band spacing, resulting in localization induced higher global kinematic hardening and increase of grain boundary stress concentrations. Our efficient explicit numerical framework allowed to simulate slip bands 100 time thinner than the average grain size, which is the relevant size for clear channels in irradiated Zr alloys, within three dimensional polycrystals.

This work is intended as a first step providing qualitative insights on the potential of this modeling approach. To obtain quantitative predictions of the local and overall behavior of such materials within this framework, many improvements should be introduced. First, regarding composite voxel models, the present formulation should be extended to finite strain in order to handle the large deformations involved when simulating strain localization. Second, more than one family of slip planes should be accounted for, raising some difficulties in handling slip band intersections regarding the definition of composite voxels. Third, a realistic physics-based model of the plasticity of irradiated metals should be introduced for the material behavior inside slip bands. And finally, similar studies should be conducted on statistically representative polycrystalline aggregates.

## Acknowledgements

The authors are grateful to Samuel Forest and Fabien Onimus for fruitful discussions, and wish to thank Julien Derouillat and Jérémy Duvergé for their involvement in the development of the AMITEX\_FFTP simulation software.

## References

Ahmed, J., Wilkinson, A.J., Roberts, S.G., 2001. Electron channelling contrast imaging characterization of dislocation structures associated with extrusion and intrusion systems and fatigue cracks in copper single crystals. *Philosophical Magazine A* 81, 1473–1488. doi:[10.1080/01418610108214358](https://doi.org/10.1080/01418610108214358).

- Anderson, D., 1965. Iterative procedures for nonlinear integral equations. *J. Assoc. Comput. Mach.* 12, 547–560. doi:[10.1145/321296.321305](https://doi.org/10.1145/321296.321305).
- Asaro, R., Rice, J., 1977. Strain localization in ductile single crystals. *Journal of the Mechanics and Physics of Solids* 25, 309–338. doi:[10.1016/0022-5096\(77\)90001-1](https://doi.org/10.1016/0022-5096(77)90001-1).
- Bapna, M., Meshii, M., 1974. Deformation of quench-hardened gold crystals. *Materials Science and Engineering* 16, 181–191. doi:[https://doi.org/10.1016/0025-5416\(74\)90152-9](https://doi.org/10.1016/0025-5416(74)90152-9).
- Barton, N., Arsenlis, A., Marian, J., 2013. A polycrystal plasticity model of strain localization in irradiated iron. *Journal of the Mechanics and Physics of Solids* 61, 341–351. doi:[10.1016/j.jmps.2012.10.009](https://doi.org/10.1016/j.jmps.2012.10.009).
- Bridier, F., Villechaise, P., Mendez, J., 2008. Slip and fatigue crack formation processes in an  $\alpha/\beta$  titanium alloy in relation to crystallographic texture on different scales. *Acta Materialia* 56, 3951 – 3962. doi:<https://doi.org/10.1016/j.actamat.2008.04.036>.
- Byun, T., Hashimoto, N., Farrell, K., 2006. Deformation mode map of irradiated 316 stainless steel in true stress-dose space. *Journal of Nuclear Materials* 351, 303–315. doi:[10.1016/j.jnucmat.2006.02.033](https://doi.org/10.1016/j.jnucmat.2006.02.033).
- Charière, R., Marano, A., Gélébart, 2020. Use of composite voxels in fft based elastic simulations of hollow glass microspheres/polypropylene composites. *International Journal of Solids and Structures* 182-183, 1 – 14. URL: <http://www.sciencedirect.com/science/article/pii/S0020768319303531>, doi:<https://doi.org/10.1016/j.ijsolstr.2019.08.002>.
- Chen, Y., Gélébart, L., Chateau, C., Bornert, M., Sauder, C., King, A., 2019. Analysis of the damage initiation in a sic/sic composite tube from a direct comparison between large-scale numerical simulation and synchrotron x-ray micro-computed tomography. *International Journal of Solids and Structures* 161, 111 – 126. doi:<https://doi.org/10.1016/j.ijsolstr.2018.11.009>.
- Dao, M., Asaro, R.J., 1996a. Localized deformation modes and non-schmid effects in crystalline solids. part i. critical conditions of localization. *Mechanics of Materials* 23, 71 – 102. URL: <http://www.sciencedirect.com>.

[com/science/article/pii/0167663696000129](http://www.sciencedirect.com/science/article/pii/S0022311513007083), doi:[https://doi.org/10.1016/0167-6636\(96\)00012-9](https://doi.org/10.1016/0167-6636(96)00012-9).

Dao, M., Asaro, R.J., 1996b. Localized deformation modes and non-schmid effects in crystalline solids. part ii. deformation patterns. *Mechanics of Materials* 23, 103 – 132.

Erinosho, T., Dunne, F., 2015. Strain localization and failure in irradiated zircaloy with crystal plasticity. *International Journal of Plasticity* 71, 170–194. doi:[10.1016/j.ijplas.2015.05.008](https://doi.org/10.1016/j.ijplas.2015.05.008).

Fong, R., 2013. Anisotropy factors from texture and mechanical strain in zircaloy-4 fuel sheaths. *Journal of Nuclear Materials* 440, 288 – 297. URL: <http://www.sciencedirect.com/science/article/pii/S0022311513007083>, doi:<https://doi.org/10.1016/j.jnucmat.2013.04.089>.

Forest, S., 1998. Modeling slip, kink and shear banding in classical and generalized single crystal plasticity. *Acta Materialia* 46, 3265–3281. doi:[10.1016/S1359-6454\(98\)00012-3](https://doi.org/10.1016/S1359-6454(98)00012-3).

Gélébart, Ouaki, F., 2015. Filtering material properties to improve fft-based methods for numerical homogenization. *Journal of Computational Physics* 294, 90 – 95. URL: <http://www.sciencedirect.com/science/article/pii/S002199911500203X>, doi:<https://doi.org/10.1016/j.jcp.2015.03.048>.

Gélébart, L., Mondon-Cancel, R., 2013. Non-linear extension of fft-based methods accelerated by conjugate gradients to evaluate the mechanical behavior of composite materials. *Computational Materials Science* 77, 430 – 439. URL: <http://www.sciencedirect.com/science/article/pii/S0927025613002188>, doi:<https://doi.org/10.1016/j.commatsci.2013.04.046>.

Helfer, T., Michel, B., Proix, J.M., Salvo, M., Sercombe, J., 2015. Introducing the open-source MFront code generator: Application to mechanical behaviours and material knowledge management within the PLEIADES fuel element modelling platform. *Computer and Mathematics with Applications* 70, 994–1023. doi:<https://doi.org/10.1016/j.camwa.2015.06.027>.

- Hure, J., Shawish, S.E., Cizelj, L., Tanguy, B., 2016. Intergranular stress distributions in polycrystalline aggregates. *Journal of Nuclear Materials* 476, 231–242. doi:[10.1016/j.jnucmat.2016.04.017](https://doi.org/10.1016/j.jnucmat.2016.04.017).
- Jaoul, B., 1964. Etude de la plasticité et application aux métaux. Les Presses - Mines ParisTech.
- Jiao, Z., Was, G., 2011. Impact of localized deformation on IASCC in austenitic stainless steels. *Journal of Nuclear Materials* 408, 246–256. doi:[10.1016/j.jnucmat.2010.10.087](https://doi.org/10.1016/j.jnucmat.2010.10.087).
- Kabel, M., Böhlke, T., Schneider, M., 2014. Efficient fixed point and newton–krylov solvers for fft-based homogenization of elasticity at large deformations. *Computational Mechanics* 54, 1497–1514. URL: <http://dx.doi.org/10.1007/s00466-014-1071-8>, doi:[10.1007/s00466-014-1071-8](https://doi.org/10.1007/s00466-014-1071-8).
- Kabel, M., Fink, A., Schneider, M., 2017. The composite voxel technique for inelastic problems. *Computer Methods in Applied Mechanics and Engineering* 322, 396 – 418. URL: <http://www.sciencedirect.com/science/article/pii/S0045782516317881>, doi:<https://doi.org/10.1016/j.cma.2017.04.025>.
- Kabel, M., Merkert, D., Schneider, M., 2015. Use of composite voxels in fft-based homogenization. *Computer Methods in Applied Mechanics and Engineering* 294, 168 – 188. URL: <http://www.sciencedirect.com/science/article/pii/S0045782515001954>, doi:<https://doi.org/10.1016/j.cma.2015.06.003>.
- Kabel, M., Ospald, F., Schneider, M., 2016. A model order reduction method for computational homogenization at finite strains on regular grids using hyperelastic laminates to approximate interfaces. *Computer Methods in Applied Mechanics and Engineering* 309, 476 – 496. URL: <http://www.sciencedirect.com/science/article/pii/S0045782516306077>, doi:<https://doi.org/10.1016/j.cma.2016.06.021>.
- Kearns, J., 1965. Thermal expansion and preferred orientation in zircaloy, in: LWBR Development Program.

- Korbel, A., Embury, J., Hatherly, M., Martin, P., Erbsloh, H., 1986. Microstructural aspects of strain localization in al-mg alloys. *Acta Metallurgica* 34, 1999 – 2009. doi:[https://doi.org/10.1016/0001-6160\(86\)90259-2](https://doi.org/10.1016/0001-6160(86)90259-2).
- Korbel, A., Martin, P., 1986. Microscopic versus macroscopic aspect of shear bands deformation. *Acta Metallurgica* 34, 1905 – 1909. doi:[https://doi.org/10.1016/0001-6160\(86\)90249-X](https://doi.org/10.1016/0001-6160(86)90249-X).
- Korbel, A., Martin, P., 1988. Microstructural events of macroscopic strain localization in prestrained tensile specimens. *Acta Metallurgica* 36, 2575 – 2586. doi:[https://doi.org/10.1016/0001-6160\(88\)90202-7](https://doi.org/10.1016/0001-6160(88)90202-7).
- Lai, M., Tasan, C., Raabe, D., 2015. Deformation mechanism of omega-enriched Ti–Nb-based gum metal : Dislocation channeling and deformation induced omega–beta transformation. *Acta Materialia* 100, 290–300. doi:<http://dx.doi.org/10.1016/j.actamat.2015.08.047>.
- Luft, A., 1991. Microstructural processes of plastic instabilities in strengthened metals. *Progress in Materials Science* 35, 97 – 204. URL: <http://www.sciencedirect.com/science/article/pii/007964259190002B>, doi:[https://doi.org/10.1016/0079-6425\(91\)90002-B](https://doi.org/10.1016/0079-6425(91)90002-B).
- Marano, A., Gélébart, L., Forest, S., 2019. Intragranular localization induced by softening crystal plasticity: Analysis of slip and kink bands localization modes from high resolution fft-simulations results. *Acta Materialia* 175, 262 – 275. doi:<https://doi.org/10.1016/j.actamat.2019.06.010>.
- Mareau, C., Robert, C., 2017. Different composite voxel methods for the numerical homogenization of heterogeneous inelastic materials with fft-based techniques. *Mechanics of Materials* 105, 157 – 165.
- Mori, T., Meshii, M., 1969. Plastic deformation of quench-hardened aluminium single crystals. *Acta Metallurgica* 17, 167–175. doi:[10.1016/0001-6160\(69\)90137-0](https://doi.org/10.1016/0001-6160(69)90137-0).
- Moulinec, H., Suquet, P., 1998. A numerical method for computing the overall response of nonlinear composites with complex microstructure. *Comput. Methods Appl. Mech. Engrg.* 157, 69–94. doi:[10.1016/S0045-7825\(97\)00218-1](https://doi.org/10.1016/S0045-7825(97)00218-1).

- Neeraj, T., Hou, D.H., Daehn, G., Mills, M., 2000. Phenomenological and microstructural analysis of room temperature creep in titanium alloys. *Acta Materialia* 48, 1225 – 1238. doi:[https://doi.org/10.1016/S1359-6454\(99\)00426-7](https://doi.org/10.1016/S1359-6454(99)00426-7).
- Neuhäuser, H., 1983. Dislocation in solids. ed. F.R.N. Nabarro. Holland Publishing Company Vol. 6,, 319–440.
- Onchi, T., Kanayo, H., Higashiguchi, Y., 1977. Effect of neutron irradiation on deformation behavior of zirconium. *Journal of Nuclear Science and Technology* 14, 359–369. URL: <http://dx.doi.org/10.1080/18811248.1977.9730770>, doi:[10.1080/18811248.1977.9730770](https://doi.org/10.1080/18811248.1977.9730770).
- Onimus, F., Bechade, J., 2009. A polycrystalline modeling of the mechanical behavior of neutron irradiated zirconium alloys. *Journal of Nuclear Materials* 384, 163–174. doi:[10.1016/j.jnucmat.2008.11.006](https://doi.org/10.1016/j.jnucmat.2008.11.006).
- Onimus, F., Béchade, J.L., Gilbon, D., 2012. Experimental analysis of slip systems activation in neutron-irradiated zirconium alloys and comparison with polycrystalline model simulations. *Metallurgical and Materials Transactions A* 44, 45–60. URL: <http://dx.doi.org/10.1007/s11661-012-1463-3>, doi:[10.1007/s11661-012-1463-3](https://doi.org/10.1007/s11661-012-1463-3).
- Onimus, F., Monnet, I., Béchade, J., Prioul, C., Pilvin, P., 2004. A statistical TEM investigation of dislocation channeling mechanism in neutron irradiated zirconium alloys. *Journal of Nuclear Materials* 328, 165–179. doi:[10.1016/j.jnucmat.2004.04.337](https://doi.org/10.1016/j.jnucmat.2004.04.337).
- Patra, A., McDowell, D., 2012. Crystal plasticity-based constitutive modelling of irradiated BCC structures. *Philosophical Magazine* 92:7, 861–887. doi:[10.1080/14786435.2011.634855](https://doi.org/10.1080/14786435.2011.634855).
- Patra, A., McDowell, D., 2016. Crystal plasticity investigation of the microstructural factors influencing dislocation channeling in a model irradiated bcc material. *Acta Materialia* 110, 364–376. doi:[10.1016/j.actamat.2016.03.041](https://doi.org/10.1016/j.actamat.2016.03.041).
- Pawlik, K., 1986. Determination of the orientation distribution function from pole figures in arbitrarily defined cells. *physica status solidi (b)* 134, 477–483. URL: <https://onlinelibrary.wiley.com/>

[doi/abs/10.1002/pssb.2221340205](https://doi.org/10.1002/pssb.2221340205), [doi:10.1002/pssb.2221340205](https://doi.org/10.1002/pssb.2221340205),  
[arXiv:https://onlinelibrary.wiley.com/doi/pdf/10.1002/pssb.2221340205](https://arxiv.org/abs/https://onlinelibrary.wiley.com/doi/pdf/10.1002/pssb.2221340205).

Pokor, C., Averty, X., Bréchet, Y., Dubuisson, P., Massoud, J., 2004. Effect of irradiation defects on the work hardening behavior. *Scripta Materialia* 50, 597 – 600. URL: <http://www.sciencedirect.com/science/article/pii/S1359646203007590>, doi:<https://doi.org/10.1016/j.scriptamat.2003.11.029>.

Robert, C., Mareau, C., 2015. A comparison between different numerical methods for the modeling of polycrystalline materials with an elastic-viscoplastic behavior. *Computational Materials Science* 103, 134 – 144.

Sauzay, M., Bavard, K., Karlsen, W., 2010. Tem observations and finite element modelling of channel deformation in pre-irradiated austenitic stainless steels – interactions with free surfaces and grain boundaries. *Journal of Nuclear Materials* 406, 152 – 165. URL: <http://www.sciencedirect.com/science/article/pii/S0022311510000838>, doi:<https://doi.org/10.1016/j.jnucmat.2010.01.027>. fP6 IP PERFECT Project: Prediction of Irradiation Damage Effects in Reactor Components.

Schneider, M., Merkert, D., Kabel, M., 2017. FFT-based homogenization for microstructures discretized by linear hexahedral elements. *International journal for numerical methods in engineering* 109, 1461–1489. doi:[10.1002/nme.5336](https://doi.org/10.1002/nme.5336).

Sharp, J., 1972. Correlation between cleared channels and surface slip steps in neutron irradiated copper crystals. *Radiation Effects* 14, 71–75. doi:[10.1080/00337577208230474](https://doi.org/10.1080/00337577208230474).

Sluys, L., Estrin, Y., 2000. The analysis of shear banding with a dislocation based gradient plasticity model. *International Journal of Solids and Structures* 37, 7127 – 7142.

Ulmer, D., Altstetter, C., 1991. Hydrogen-induced strain localization and failure of austenitic stainless steels at high hydrogen concentrations. *Acta Metallurgica et Materialia* 39, 1237–1248. doi:[https://doi.org/10.1016/0956-7151\(91\)90211-I](https://doi.org/10.1016/0956-7151(91)90211-I).

- Willot, F., 2015. Fourier-based schemes for computing the mechanical response of composites with accurate local fields. *Comptes Rendus Mécanique* 343, 232 – 245. URL: <http://www.sciencedirect.com/science/article/pii/S1631072114002149>, doi:<https://doi.org/10.1016/j.crme.2014.12.005>.
- Wisner, S., Reynolds, M., Adamson, R., 1994. Fatigue behavior of irradiated and unirradiated zircaloy and zirconium. *Zirconium in the Nuclear Industry: Tenth International Symposium* , 499–499–22URL: <http://dx.doi.org/10.1520/STP15206S>, doi:[10.1520/stp15206s](https://doi.org/10.1520/stp15206s).
- Xiao, X., Song, D., Xue, J., Chu, H., Duan, H., 2015. A size-dependent tensorial plasticity model for FCC single crystals with irradiation. *International Journal of Plasticity* 65, 152–167. doi:[10.1016/j.ijplas.2014.09.004](https://doi.org/10.1016/j.ijplas.2014.09.004).
- Zhang, M., Bridier, F., Villechaise, P., Mendez, J., McDowell, D., 2010. Simulation of slip band evolution in duplex ti–6al–4v. *Acta Materialia* 58, 1087 – 1096. URL: <http://www.sciencedirect.com/science/article/pii/S1359645409007198>, doi:<https://doi.org/10.1016/j.actamat.2009.10.025>.